



### **Science Arts & Métiers (SAM)**

is an open access repository that collects the work of Arts et Métiers Institute of Technology researchers and makes it freely available over the web where possible.

This is an author-deposited version published in: <https://sam.ensam.eu>  
Handle ID: <http://hdl.handle.net/10985/19566>

#### **To cite this version :**

X. XU, D.J. ALLEN, M.A.E. JEPSON, W. SUN, Adil BENAARBIA - Investigation of microstructural evolution and creep rupture behaviour of 9% Cr MarBN steel welds - Materials Science and Engineering: A - Vol. 791, p.139546 - 2020

Any correspondence concerning this service should be sent to the repository

Administrator : [scienceouverte@ensam.eu](mailto:scienceouverte@ensam.eu)



# **Investigation of microstructural evolution and creep rupture behaviour of 9% Cr MarBN steel welds**

X. Xu<sup>\*1</sup>, A. Benaarbia<sup>2</sup>, D. Allen<sup>1</sup>, Mark A. E. Jepson<sup>1</sup>, W. Sun<sup>3</sup>

<sup>1</sup> Department of Materials, Loughborough University, Loughborough, Leicestershire  
LE11 3TU, UK

<sup>2</sup> Arts et Métiers, CNRS, Université de Lorraine, LEM3, F-57000 Metz, France

<sup>3</sup> Department of Mechanical, Materials and Manufacturing Engineering, University of  
Nottingham, Nottingham, Nottinghamshire, NG7 2RD, UK

## **ABSTRACT**

The weldments made from the 9-12% Cr tempered martensitic steel are associated with a complex microstructure arising from complicated thermal histories of the fusion and heat affected zones. The complicated microstructural and micro-mechanical states in these critical regions provide a challenge for the determination of creep failure mechanisms. Based on detailed metallographic examination, the microstructural distribution in the heat affected zone of the welds constructed using a recently developed 9% Cr MarBN steel, IBN-1, has been identified and classified into Equiaxed Zone (EZ), Duplex Zone (DZ) and Over-tempered Zone (OZ). Cross-weld testing performed at 650°C has revealed a significant reduction in creep life as compared to bulk material. Creep rupture has been shown to occur in the parent metal region with a ductile manner at a high stress, whereas creep rupture initiates in the DZ region in an intergranular manner at a low stress. Detailed metallographic investigation has further revealed a higher damage susceptibility in the regions along the pre-existing Prior Austenite Grain Boundaries (PAGBs). The diffusional reaustenitisation of local microstructure along the PAGBs leads to a lower strength of matrix in combination with a lack of intergranular

precipitates as compared to the surrounding microstructure formed after displacive  
reaustenitisation.

**KEYWORDS:** 9% Cr tempered martensitic steel; heat affected zone; multi-pass welding;  
high temperature creep; failure mechanism

## **1. INTRODUCTION**

The 9-12% Cr creep resistant martensitic steels are widely used in high temperature  
pressure vessels and piping for the power generation industry due to their good  
combination of creep strength and oxidation resistance. Based on a nominal composition  
of Fe-9%Cr-3%W-3%Co-VNbBN [1], variants of Martensitic steel strengthened by  
boron and nitrogen (MarBN) have been recently developed to replace the more  
conventional 9% Cr materials such as the Grade 91 and 92 steels by providing superior  
creep performance in combination with sufficient oxidation resistance [2]. During recent  
years, the major developments based on the concept of MarBN include a range of  
materials originating from international collaborative research activities including the  
G115 (China), SAVE12AD (Japan), NPM-1 (Europe) and the IBN-1 (UK) steels [3–6].  
These materials are typically manufactured by using common industrial processes  
finished with normalisation and tempering to produce a tempered martensitic  
microstructure in combination with secondary precipitates distributed both on grain  
boundaries and within the grain interiors [1]. These MarBN steels are also compatible  
with a variety of fusion welding processes including Manual Metal Arc Welding  
(MMAW), Submerged Arc Welding (SAW) and Gas Tungsten Arc Weld (GTAW).  
Multi-pass welding processes have been used to fabricate welds on MarBN steels to  
achieve sufficient ductility in the weld metal and the Heat Affected Zone (HAZ).

Interest in the creep performance of welds fabricated in 9-12% Cr steels is increasing due to their potential applications in power plant systems. The evaluation of welded joint behaviour during creep exposure is a key factor in determining the lifetime of power plant components. The existing studies of cross-weld samples under creep conditions have shown that the ratio of creep rupture strength between cross-welds and the parent material depends on both creep loading conditions and welding procedure [7]. At low testing temperatures there is no large difference between parent metal and cross-weld creep strength, whilst this difference becomes important at high temperatures and low stress levels. Additionally, rupture locations were found to shift from the weld metal to the HAZ as the applied stress decreased [8]. No substantial differences were found in the minimum creep rate, the time to fracture and creep ductility for the cross-weld specimens taken from different locations of the weld [8].

The welds fabricated in 9-12% Cr steels are associated with premature creep failure within the HAZ, typically termed as 'Type IV' failure [9]. Type IV failure is commonly presented in the HAZ region close to the boundary with the parent metal and causes a substantial loss in creep strength for weldments as compared to bulk materials [10,11]. Detailed metallographic examination conducted on interrupted creep test specimens has revealed the presence of creep cavities prior to final rupture in a Type IV manner [12]. Based on extensive metallographic examination, the metallurgical cause for the formation of creep cavities is complicated and linked with a range of factors relating to the microstructure of 9-12% Cr steels. For instance, the presence of second phase particles (e.g. boron nitride, BN) above a critical size has been determined as a critical issue that promotes the formation of cavities from the early stage of creep [12,13]. The presence of Type IV failure in 9-12% Cr steels is also related with a layer of HAZ material exhibiting

a refined martensitic microstructure in combination with a lack of precipitate formation on lath and grain boundaries [14,15]. However, most of the existing studies are conducted using welds made from conventional materials such as Grade 91 and 92 steels, whilst the research focused on the creep failure mechanism of recently developed MarBN steels is comparatively limited.

Detailed investigation of the creep failure mechanism of 9-12% Cr steel welds is also challenging due to a complicated HAZ microstructure formed by the complex thermal distribution established during multi-pass welding. Extensive research has been conducted using experimental measurement and numerical modelling techniques to understand the thermal distribution in the HAZ [16–18]. These studies reveal that the thermal history of the HAZ is typically composed of a heating phase with a heating rate of  $>100^{\circ}\text{C/s}$  and a subsequent cooling phase during which temperature decreases to the ambient level within tens of seconds [16,17]. The variation of the microstructure in the HAZ has been further correlated with thermal distribution based on detailed metallographic examination and dilatometry simulation in 9-12% Cr steels as reported in [19,20]. Detailed previous studies conducted on a more conventional Grade 92 alloy have classified the HAZ microstructure into three critical sub-regions: Completely Transformed Zone (CTZ), Partially Transformed Zone (PTZ) and Over-Tempered Zone (OTZ) based on the range of peak temperatures reached during weld thermal cycles [20]. A more recent study based on the dilatometry simulation of a MarBN steel, IBN-1, has further determined a similar trend of variation in the HAZ microstructure as a function of peak temperature [21]. However, there is a lack of direct, systematic investigations from the weld HAZs to correlate with the presence of creep damage in MarBN steels.

In the current research, the microstructural distribution in the HAZ of welds in a parent metal of the MarBN steel, IBN-1, has been investigated in detail in the initial state without creep exposure. The mechanical behaviour of the IBN-1 welds has been further investigated upon short-term creep exposure using cross-weld specimens at 650°C to compare with the bulk materials tested at similar testing conditions. Detailed metallographic examinations have been subsequently performed to identify the critical metallurgical factors related to the formation of creep damage after rupture at different stress levels.

## 2. MATERIAL AND EXPERIMENTAL METHODS

### 2.1. Materials

The chemical composition of the IBN-1 steel used (referred as parent metal) is listed in Table 1. The initial heat treatment of the parent metal involved a normalisation process at 1200°C for 4 hours and a tempering process at 765°C for 3 hours. A butt weld was then fabricated between the plates of parent metal that are ~30 mm in thickness by using a multi-pass MMAW process with a recently developed matching filler material, Metrode® Chromet® 933. In total, 26 weld beads were deposited with a heat input of 1.1 – 1.5 kJ/mm with the interpass temperature maintained between 200°C and 300°C. Post Weld Heat Treatment (PWHT) was conducted after welding at 760°C for 2 hours.

**Table 1. Chemical composition of the IBN-1 parent metal (wt. %, balance is Fe).**

C	Si	Mn	P	S	Cr	Mo	Ni
0.1	0.45	0.54	0.012	0.004	8.74	0.05	0.14
Al	B	Co	Cu	Nb	V	W	N
0.007	0.012	3.02	0.04	0.06	0.21	2.53	0.018

## 2.2. Creep testing

Creep test specimens were machined to a dog-bone shape with a cylindrical gauge portion measuring 50 mm in length and 10 mm in diameter. The gauge portion consists of the weld and the parent metals, together with the intermediate HAZ located at ~10 mm from the boundary between the gauge and the head portions, Figure 1. The HAZ is perpendicular to the principal stress direction to achieve a volume fraction of the weld metal at ~20 % in the gauge portion.

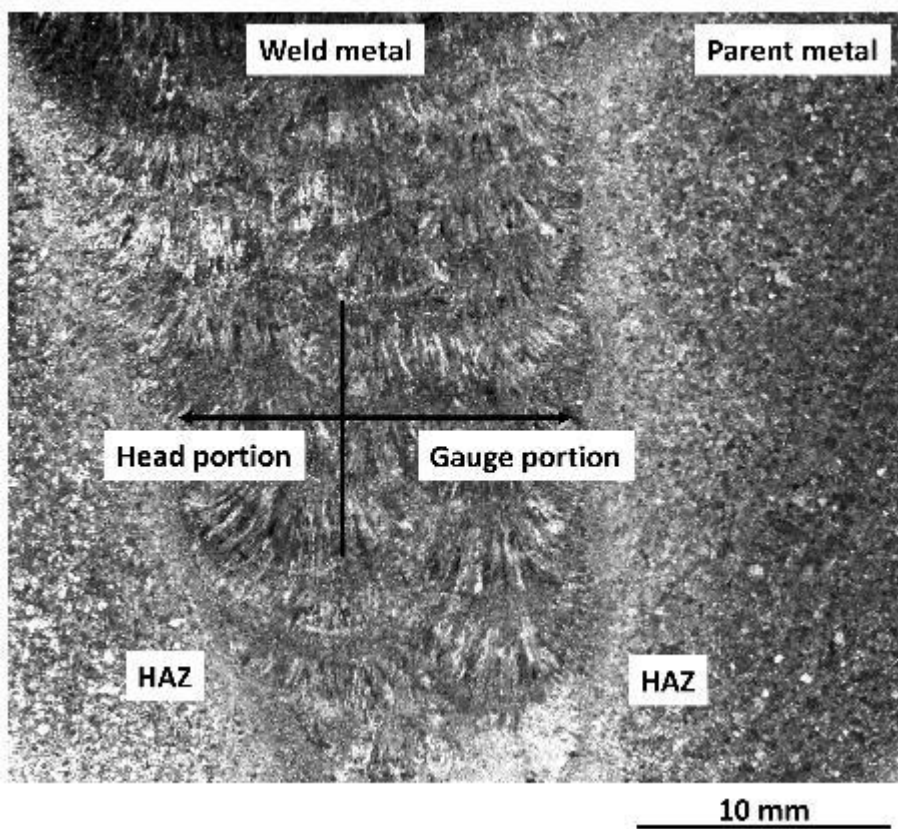


**Figure 1. Optical macrograph giving an overview of the weld structure in the cross-weld creep specimen.**

Isothermal short-term cross-weld creep tests were conducted at 650°C with a series of stress levels ranging from 160 MPa to 280 MPa. The stress levels were selected based on

the existing experience of creep testing of MarBN steel [22], such that the specimens were expected to be ruptured in different manners for a comparison in creep characteristics. The specimens tested at a stress level close to 280 MPa were expected to fracture in a ductile manner with rupture occurring in the parent metal. The specimens tested at a stress level close to 160 MPa were chosen to fracture in the HAZ.

The testing machine was equipped with high temperature Linear Variable Displacement Transformers (LVDT) to continuously monitor the elongation of specimens, and a resistance-heating furnace enabling a quasi-homogeneous testing temperature of up to 800°C. The measured creep strain represents the integral accumulated creep strain of the entire cross-weld material within the gauge length. Three thermocouples were attached to the specimen inside the furnace to track the operating temperature. Note that the thermal gradient between both sample extremities was less than 2°C. Prior to testing, thermal loading was first performed with a rate of 40°C/min until reaching the target temperature. After stabilization of the furnace temperature (~30 minutes), creep tests were conducted until the macroscopic failure of samples.

### **2.3. Metallographic examination**

Gauge portions of the creep ruptured specimens were sectioned from the head and along the longitudinal direction for detailed metallographic examination of the cross-sections. The specimens were prepared using conventional metallographic preparation methods, which involved mounting in electrically conductive Bakelite, grinding on SiC with water to a 1200 grit finish, polishing on standard polishing cloths using 6 µm and 1 µm diamond suspensions and a final chemo-mechanical polishing process using a suspension of 0.06



150  $\mu\text{m}$  colloidal silica in water. An as-fabricated weld was also prepared using the same  
151 procedure to provide details of the initial microstructure before creep exposure.

152 Hardness testing was conducted on the as-fabricated weld using a loading weight of 10 kg  
153 and a dwell time of 10 s using a Struers® Durascan® 70 hardness testing system equipped  
154 with a Vickers indenter. Seven individual measurements were conducted to obtain the  
155 average value of hardness from both the weld and the parent metals. Hardness mapping  
156 was also undertaken on the as-fabricated weld and on creep ruptured specimens in the  
157 regions adjacent to the rupture surface using a loading weight of 0.2 kg and a dwell time  
158 of 10 s using the identical hardness testing system. Vickers hardness indents were  
159 distributed on a square grid with a spacing of 0.1 mm.

160 Fractography examination was performed on the fracture surfaces of creep ruptured  
161 specimens using a JEOL® JSM-7800F Field Emission Gun (FEG) Scanning Electron  
162 Microscope (SEM) at an accelerating voltage of 5 kV. Grain orientation mapping of the  
163 matrix was undertaken by performing EBSD mapping at an accelerating voltage of 20 kV  
164 using an Oxford Instruments® Nordlys® MAX<sup>2</sup> camera in the JEOL® JSM-7800F FEG-  
165 SEM. EBSD maps were collected on the cross-section of the as-fabricated weld and  
166 adjacent to the rupture surface of creep fractured specimens at a step size of 2  $\mu\text{m}$  with a  
167 size of 1000  $\times$  1000  $\mu\text{m}$  to provide an overview of the microstructure. EBSD mapping  
168 was also performed at a finer step size of 0.1  $\mu\text{m}$  to obtain details of the microstructure.  
169 The distribution of secondary precipitates in identical regions to where EBSD mapping  
170 was conducted was characterised using ion induced Secondary Electron (SE) imaging in  
171 a FEI® Nova Nanolab® 600 Focused Ion Beam (FIB) FEG-SEM. The ion beam was  
172 operated at an accelerating voltage of 30 kV with  $\text{XeF}_2$  gas etching used to enhance the  
173 contrast differential between precipitates and matrix [19,23].

Thin-foil specimens were extracted from site-specific locations where the correlative EBSD/ion induced SE analysis was conducted using an *in-situ* lift-out technique [24] in a FEI® Nova Nanolab® 600 FIB/FEG-SEM. The thinning of specimens was performed at an accelerating voltage of 30 kV with a beam current decreasing to 0.1 nA, followed by a final cleaning process performed at an accelerating voltage of 5 kV. The extracted thin-foil specimens were investigated using Bright Field Scanning Transmission Electron Microscopy (BF-STEM) in a FEI® Tecnai® F20 Transmission Electron Microscope (TEM) at an accelerating voltage of 200 kV. Secondary precipitates were further characterised using Selected Area Electron Diffraction (SAED) in combination with Energy Dispersive X-ray (EDX) spectroscopy using an Oxford Instruments® X-Max 80<sup>N</sup> TLE EDX system.

### 3. RESULTS

#### 3.1. Microstructural distribution in the as-fabricated condition

The hardness of the weld and the parent metals were measured using macro-hardness testing. The hardness of the weld and the parent metals were determined to be  $290 \pm 4$  and  $249 \pm 2$  HV<sub>10</sub>, respectively. The value of hardness obtained from the parent metal is consistent with the previous reports from similar MarBN steels [25,26]. The weld metal exhibited a higher level of hardness as compared to the parent metal. This is possibly attributed to a more refined martensitic microstructure as formed in the weld metal after rapid solidification and cooling during the welding stage, and a less homogenised and recovered martensitic substructure due to a lack of normalisation treatment as compared to the parent metal.

The microstructural variation in the as-fabricated weld without creep exposure was further characterised using hardness mapping analysis at a different loading weight of 0.2 kg. Figure 2 demonstrates a macro optical micrograph providing an overview of the weld microstructure and a hardness map from the same region.

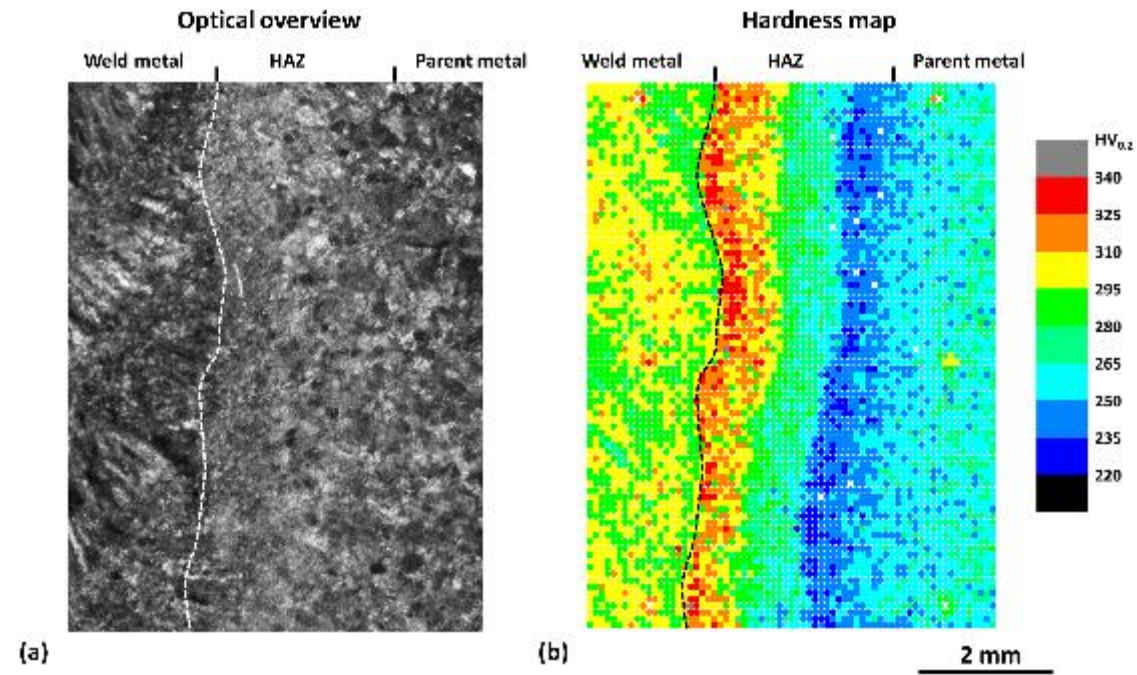


**Figure 2. (a) A macro optical micrograph demonstrating the variation of microstructure between the weld metal, the HAZ and the parent metal. (b) A hardness map showing the variation in hardness from the same region.**

From the hardness map, the weld metal has a higher level of hardness at  $296 \pm 9 \text{ HV}_{0.2}$  as compared to the parent metal measured with a hardness of  $261 \pm 9 \text{ HV}_{0.2}$ . These values of hardness are lower than the values obtained at a loading weight of 10 kg. This is attributable to the different measuring volumes that were achieved at a different loading weight. No significant variation in hardness was observed in the HAZ along the direction

parallel to the fusion boundary (i.e. from bottom to top in Figure 2), whilst a decrease in hardness was clearly observed as the distance from the fusion boundary increased. The distribution in hardness in the HAZ region suggests significant microstructural variation as a function of distance from the fusion boundary. Correlative EBSD analysis was further conducted to detail the microstructural gradient in the HAZ, Figure 3.

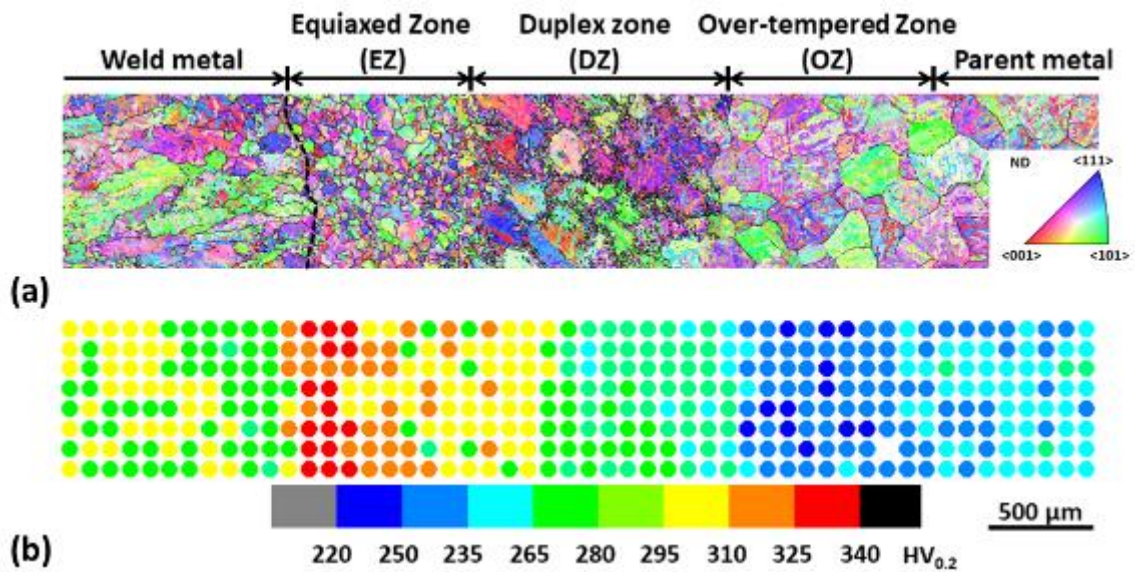


**Figure 3. (a) An EBSD map providing an overview of the tempered martensitic matrix in as-fabricated IBN-1 weld. The grain boundaries with a misorientation range between 20° and 50° are outlined by solid lines. (b) A correlative hardness map showing the variation of hardness in the identical region is also included for comparison.**

Due to a Kurdjumov-Sachs orientation relationship preserved between the martensitic ( $\alpha'$ ) and the parental austenitic ( $\gamma$ ) phases during martensitic transformation, the austenitic grain structure was characterised from EBSD maps using a boundary misorientation range between 20° and 50° [20,27,28]. Figure 3a shows that columnar and equiaxed

austenitic structures are presented in the weld and the parent metals, respectively. The columnar grains in the weld metal are typically 50-200  $\mu\text{m}$  in width and over 1000  $\mu\text{m}$  in length, whilst the equiaxed grains in the parent metal are predominantly 100-500  $\mu\text{m}$  in diameter. In the HAZ region close to the fusion boundary, the grain structure was found to have transformed from a refined, equiaxed morphology in the region <1 mm from the fusion boundary to a duplex grain structure containing small austenite grain ‘necklaces’ around pre-existing PAGBs in the region 1-2 mm from the fusion boundary. The equiaxed grains in the region <1 mm from the fusion boundary are predominantly <150  $\mu\text{m}$  in diameter, whereas the austenite “necklace” grains on the initial PAGBs are <20  $\mu\text{m}$  in diameter in the regions 1-2 mm from the fusion boundary. The microstructural gradient in the HAZ was further correlated with the variation in hardness as demonstrated in Figure 3b. The hardness map demonstrates that the region with a refined, equiaxed grain structure has a higher level of hardness measuring  $305 \pm 16 \text{ HV}_{0.2}$ , whereas the region showing a duplex grain structure has a lower level of hardness of  $262 \pm 17 \text{ HV}_{0.2}$ . The grain structure in the regions ~2-3 mm from the fusion boundary is not significantly varied from the parent metal, whereas the hardness was lower, with an average value measuring  $247 \pm 9 \text{ HV}_{0.2}$ .

The microstructure in the HAZ of as-fabricated IBN-1 weld is further correlated with the microstructure produced by the simulation of weld thermal cycles as previously reported in [21], Table 2.

**Table 2. A comparison in microstructure between the HAZ of the as-fabricated IBN-1 weld and the simulated HAZ material produced using dilatometry-based simulations of weld thermal cycle [21].**

Simulated HAZ material [21]		As-fabricated weld		Classification
Peak temperature	Characteristics of microstructure	Distance from fusion boundary	Characteristics of microstructure	
>1200°C	Equiaxed morphology, grain size <100 µm;	<1 mm	Equiaxed morphology, grain size <150 µm;	Equiaxed Zone (EZ)
1000 - 1200°C	Duplex microstructure characterised by refined grains on the pre-existing PAGBs;	1 - 2 mm	Duplex microstructure characterised by small grains (<20 µm) on the pre-existing PAGBs;	Duplex Zone (DZ)
<1000°C	Equiaxed morphology, grain size >300 µm;	2 - 3 mm	Equiaxed morphology, grain size 100 - 500 µm;	Over-tempered Zone (OZ)

Table 2 demonstrates that the distribution of HAZ microstructure as a function of the distance from fusion boundary is in strong agreement with the microstructure in the HAZ simulated materials as a function of peak temperature. This suggests that the microstructure in the weld HAZ can be classified based on the gradient of heat input as a function of the distance from fusion boundary. As a result, the weld HAZ was classified as three critical sub-regions, the Equiaxed Zone (EZ), the Duplex Zone (DZ) and the Over-tempered Zone (OZ) (Figure 3). A detailed description of the microstructure in these sub-regions is not the focus of the investigation in the current research, as this has been reported elsewhere in a previous study [21]. However, it has been clearly demonstrated in the current research that the microstructure of the HAZ in MarBN steel welds is different from the conventional understanding of the HAZs in low alloy Cr-Mo steels, which are commonly classified into Coarse-grain (CG), Fine-grain (FG), Inter-critical (IC) and Over-tempered (OT) regions [11].

### 3.2 Mechanical behaviour

Creep responses for cross-weld specimens are compared with the parent metal specimens as previously reported in [22], Figure 4. The corresponding creep properties are

summarised in Table 3. These include the Steady-State Creep Rate (SSCR), the time to fracture  $\tau_f$ , ductility  $\epsilon_f$ , and the Reduction of Area (RA).

It can be seen that the three typical creep stages (a primary creep stage followed by an apparently steady-state creep deformation and an accelerating tertiary creep stage) are clearly visible for all tests under investigation. The creep results demonstrate that the minimum creep strain rate increases with the increase of stress while creep rupture time decreases as stress increased. At the medium stress level of 200 MPa and 220 MPa, SSCR values for cross-weld are 26-fold higher than the parent metal, whilst the time to rupture is 14- to 18-fold shorter as compared to the parent metal. This clearly indicates a lower creep resistance of the cross-weld specimen as compared to the parent metal specimen. This finding applies to all stress levels selected for this investigation. Moreover, no significant changes have been observed when comparing both values of the area reduction and ductility reported for both parent metal and cross-weld.

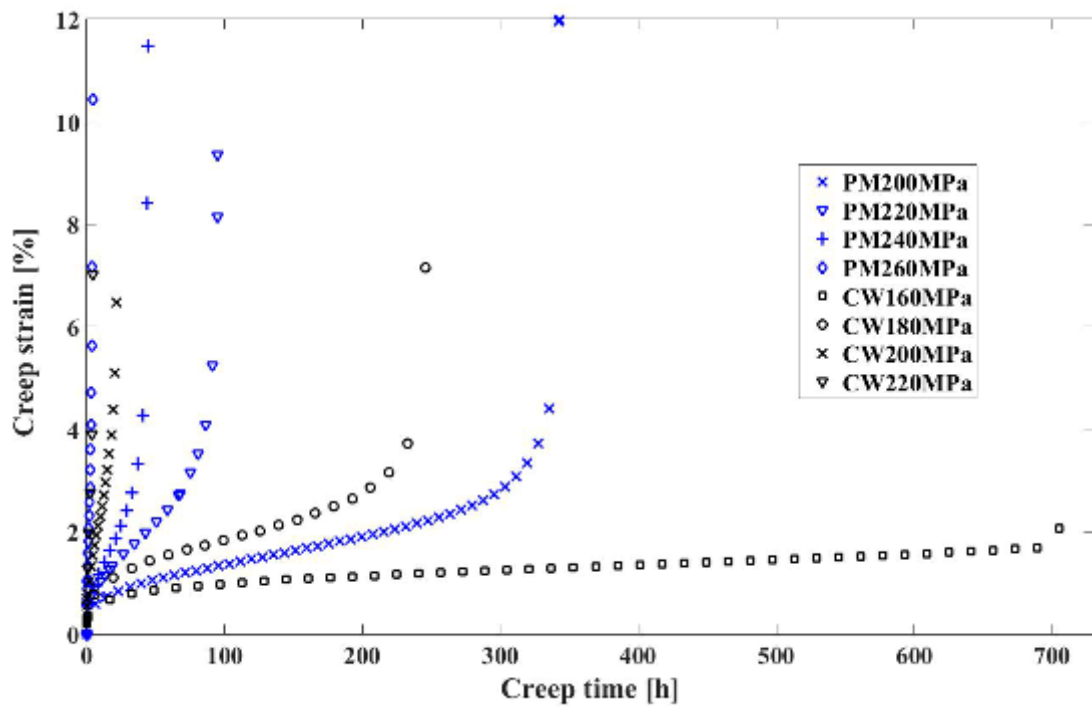


**Figure 4. Strain-time curves for creep tests conducted on parent metal (PM) and cross-weld (CW) specimens at 650°C.**

**Table 3. Material creep properties for parent metal (PM) and cross-weld (CW) specimens selected at different stress levels.**

$\sigma$ [MPa]	Material	SSCR [ $10^{-5} \times h^{-1}$ ]	$\tau_f$ [h]	$\epsilon_f$ [%]	RA [%]
160	PM	-	-	-	-
	CW	1.13	705.56	2.66	14.44
180	PM	-	-	-	-
	CW	7.31	248.35	5.62	42.24
200	PM	6.12	342.91	11.93	62.05
	CW	170.02	22.96	7.86	73.79
220	PM	29.12	95.47	9.36	73.68
	CW	770.15	5.14	11.35	80.29
240	PM	280.32	13.73	11.48	74.29
	CW	-	-	-	-
260	PM	1000.21	4.43	10.48	75.11
	CW	-	-	-	-
280	PM	4851.23	0.94	14.88	81.08
	CW	-	-	-	-



All aforementioned creep rupture characteristics of the parent metal and cross-weld are gathered for comparison in Figure 5 and summarised in Table 4 in the form of power-law (relating the time-to-rupture or SSCR to the stress) and Monkman-Grant (relating the mean creep rate to SSCR) relationships. Figures 5a and 5b show that the cross-weld specimens have a considerably shorter creep life and a higher creep strain rate as compared to the parent metal specimens, whilst Figure 5c reveals a similar Monkman-Grant (MG) relationship for both the cross-weld and the parent metal specimens. In addition, no significant differences were observed for the apparent stress and MG exponents between the cross-weld and the parent metal specimens, as detailed in Table 4. The parent metal specimens show a slightly higher stress exponent value,  $m$ , as compared to the cross-weld specimen, whilst the stress exponent value,  $n$ , is slightly higher for the cross-weld specimen. The MG exponent,  $\xi$ , for the cross-weld specimens turns out to be 0.95, whilst that of the parent metal specimens is  $\sim 0.87$ .

Additional calculations were conducted on separate groups of the specimens tested at different stress levels, which appear to exhibit different creep behaviour as indicated by an evident deviation from the linear relationship as shown in Figure 5a. The stress exponent value,  $m$ , was obtained at 8.87 and 15.70 for the specimens tested at 160/180 MPa and 200/220 MPa, respectively. A close value of stress exponent,  $m$ , between the cross-weld specimens tested at a higher level of stress and the parent metal specimens suggests similar creep behaviour for the specimens tested at the identical conditions, whilst the creep behaviour of the specimens tested at 160/180 MPa may be different as proposed by a considerable discrepancy in stress exponent value with the parent metal specimens. As a result, creep life is significantly shortened to a higher extent for the cross-weld specimens tested at a lower stress level (e.g. 160 and 180 MPa).

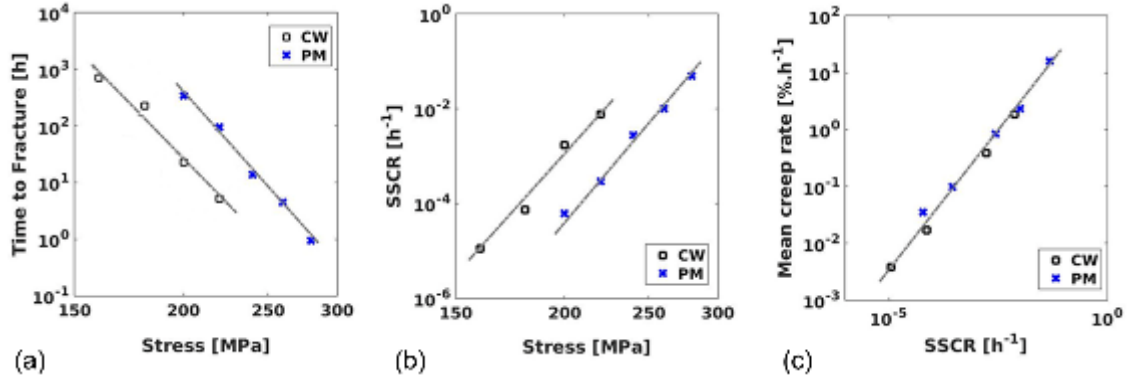


**Figure 5. (a) Time to fracture vs. applied stress. (b) SSCR vs. applied stress. (c) Mean creep rate ( $\epsilon_f/\tau_f$ ) vs. SSCR of IBN-1 cross-weld (CW) and parent metal (PM) specimens.**

**Table 4. Apparent values of creep function coefficients for parent metal (PM) and cross-weld (CW) specimens.**

Material	Time to fracture		Steady-state creep rate		Monkman-Grant relationship	
	$\tau_f = p \sigma^{-m}$		$SSCR = q \sigma^n$		$SSCR^\xi = \omega \epsilon_f/\tau_f$	
	$p [(\text{MPa})^{-1} \cdot \text{h}]$	$m [-]$	$q [(\text{MPa} \cdot \text{h})^{-1}]$	$n [-]$	$\omega [-]$	$\xi [-]$
PM	$7.59 \times 10^{42}$	17.53	$1.07 \times 10^{-50}$	19.88	0.63	0.87
CW	$2.63 \times 10^{38}$	16.08	$6.47 \times 10^{-53}$	21.42	0.56	0.95

### 3.3. Creep rupture behaviour of cross-weld specimen at different stress levels

The microstructures in the creep exposed cross-weld specimens were investigated using hardness mapping analysis in combination with fractography examination to understand the correlation between the weld microstructure and the creep rupture behaviour.

Hardness mapping was conducted in the region close to the rupture surface to reveal the variation in hardness after creep testing at 650°C and 160 MPa, Figure 6.

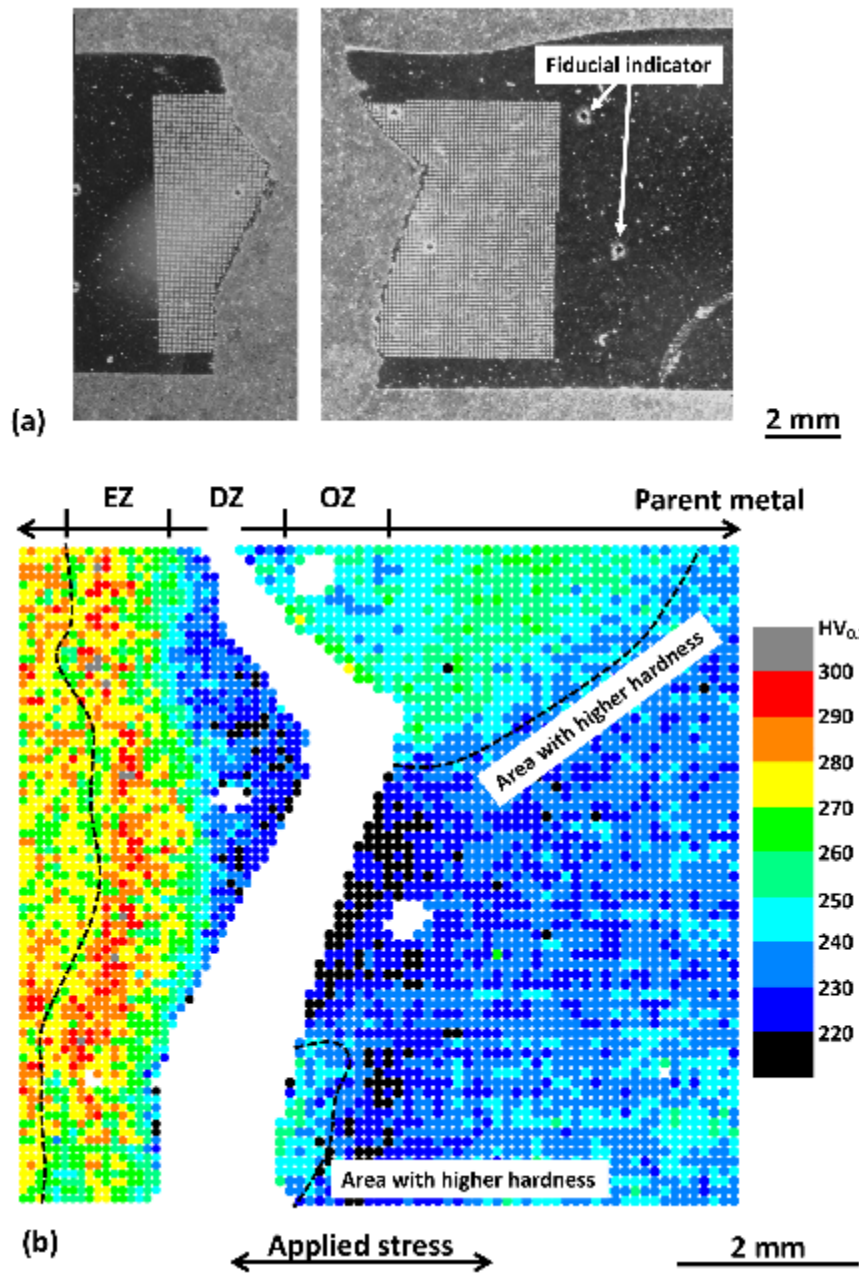
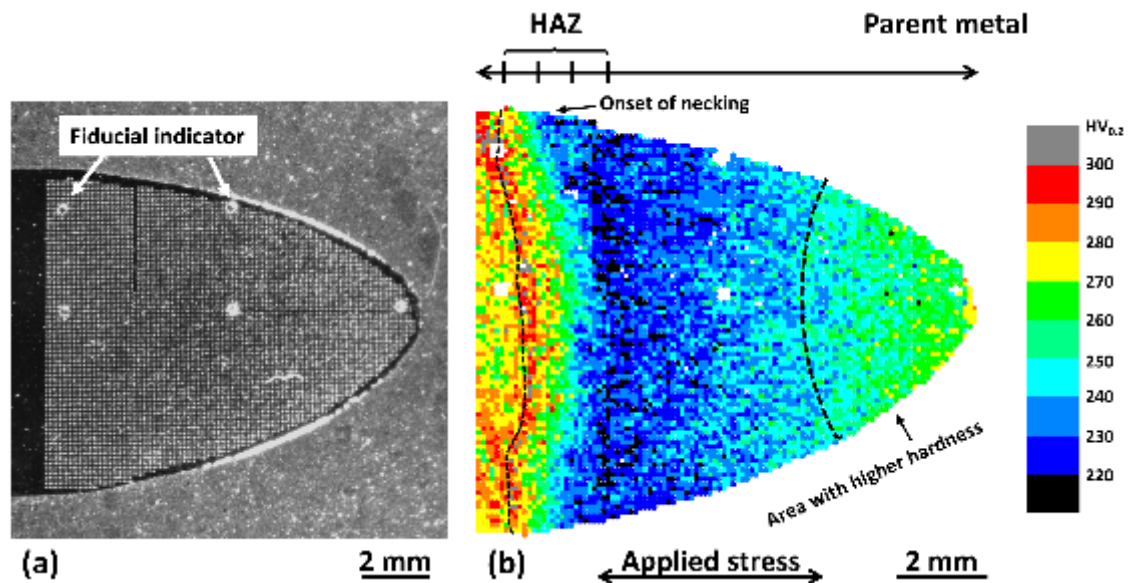


Figure 6. (a) Photographs showing the cross-section of a creep ruptured cross-weld specimen after creep testing at 650°C and 160 MPa for 705 hours prior to hardness mapping analysis. (b) A hardness map showing the variation of hardness in the region of analysis.

Figure 6b shows that the hardness of the weld metal ranges between 238 and 299 HV<sub>0.2</sub> with an average hardness measuring  $274 \pm 9$  HV<sub>0.2</sub>, whereas the hardness of the parent

327 metal is in the range of 221-258 HV<sub>0.2</sub> with an average value obtained at 236±6 HV<sub>0.2</sub>.  
328 The hardness in the HAZ decreases from 312 HV<sub>0.2</sub> to 205 HV<sub>0.2</sub> with distance from the  
329 fusion boundary. The rupture surface is located at ~1.0-2.5 mm from the fusion boundary  
330 with a zig-zag crack path. The rupture surface is aligned at ~90° to the principal stress  
331 direction close to the outer surface (bottom), whereas it is ~70° and ~45° to the principal  
332 stress direction in the centre and close to the other side (top), respectively. The hardness  
333 in the regions extending from the portions at ~90° and ~45° is in the range of 232-253  
334 HV<sub>0.2</sub> and 235-273 HV<sub>0.2</sub>, respectively. The hardness measured from the regions  
335 extending from the portion at ~70° to the principal stress direction is lower and in the  
336 range between 206 and 237 HV<sub>0.2</sub>. The angle of the rupture surface is related to the  
337 microstructure of the weld and the local stress state during creep testing. However, it is  
338 also affected by the other factors such as the surface condition of the specimen and the  
339 experimental condition of creep test. Detailed examination of the creep ruptured cross-  
340 weld specimen is required to reveal the underlying reasons for the rupture of specimens.

341 Hardness mapping analysis was further conducted on the creep ruptured specimen which  
342 was tested at 650°C and 200 MPa, Figure 7.



**Figure 7. (a) A photograph showing the cross-section of a creep ruptured cross-weld specimen after creep testing at 650°C and 200 MPa for 23 hours prior to hardness mapping analysis.**

The hardness measured from the weld and parent metals (Figure 7) is similar to the specimen ruptured at 160 MPa. The hardness of the weld metal is in the range between 253 and 314 HV<sub>0.2</sub> with an average value measuring  $279 \pm 9$  HV<sub>0.2</sub>, whereas the hardness of the parent metal is between 219 and 269 HV<sub>0.2</sub> with an average value obtained at  $241 \pm 8$  HV<sub>0.2</sub>. The hardness in the HAZ is similar to the specimen tested at 650°C and 160 MPa and is decreased from 320 to 205 HV<sub>0.2</sub> as the distance from the fusion boundary increases. The rupture surface is located at ~11 mm from the fusion boundary, with substantial necking which also includes an increase in hardness to a maximum value of 285 HV<sub>0.2</sub>.

Fractographic examination was conducted on the rupture surfaces to understand the fracture behaviour of the creep exposed specimens. Figure 8 demonstrates the topography of the rupture surface in the specimens tested at 650°C/160 MPa and 650°C/200 MPa.

Figures 8b-8g demonstrate that the rupture surface in the specimen tested at 650°C and 160 MPa has changed from an intergranular to a ductile dimpled topography from the regions with an angle of at ~90° to ~70° and ~45° to the principal stress direction. The intergranular surface at ~90° is not similar to the characteristics of typical faceted surfaces formed by intergranular fracture [29], but it is covered by scale-like features that are possibly formed by oxidation (Figure 8g). The dimples in the region ~70°/~45° to the principal stress direction are typically 3-10 µm in diameter and occasionally associated with inclusion particles (e.g. Figure 8c), which is consistent with the existing report of plastic damage associated with secondary phase particles [30]. The rupture surface of the specimen tested at 650°C and 200 MPa is composed of a dimpled central region in combination with a shear lip close to the outer surface (Figure 8h). Figure 8i demonstrates that the dimples in the central region are similar in size as compared to the specimen tested at 650°C and 160 MPa and occasionally associated with inclusions.

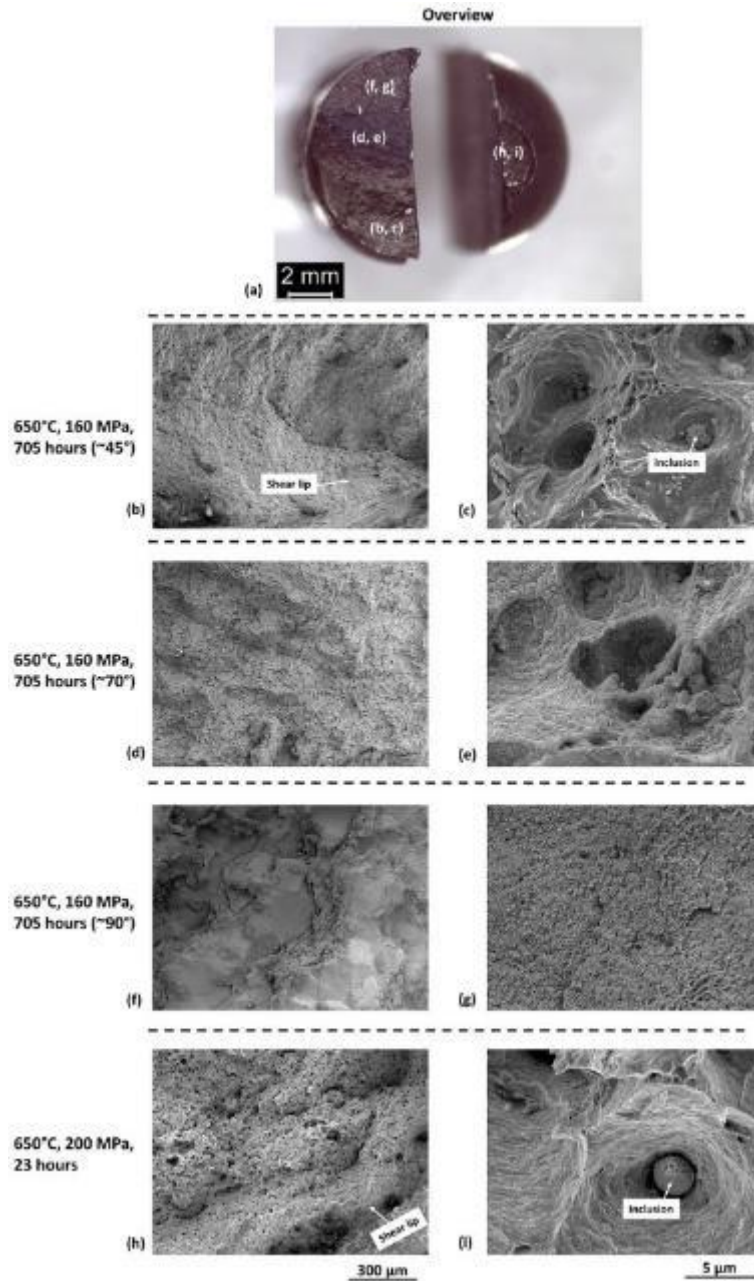


**Figure 8. (a) An optical overview of rupture surface in the specimens tested at (left) 650°C/160 MPa and (right) 650°C/200 MPa. Topography of the rupture surface is further detailed for the regions with an angle of (b, c) ~45°, (d, e) ~70° and (f, g) ~90° to the principal stress direction in the specimen tested at 650°C/160 MPa and (h, i) the rupture surface after creep testing at 650°C/200 MPa.**

Previous studies that were systematically conducted at various creep test conditions have revealed a variation in rupture behaviour from catastrophic HAZ failure occurring in the ‘Type IV’ zone, to ductile rupture of the parent metal against a decreasing testing temperature and/or an increasing stress level for the welds with a parent metal of similar materials [11,31]. This trend in creep rupture behaviour against the variation of creep test condition is consistent with the creep behaviour of IBN-1 steel welds between the tests conducted at 650°C and 160/200 MPa here. The IBN-1 weld tested at 200 MPa demonstrates similar creep behaviour to the IBN-1 parent materials from the identical industrial heat in tests at similar conditions, where dislocation climb acts as the dominant rate controlling factor for creep deformation [22]. However, the specimen tested at 650°C and 160 MPa demonstrates distinctively different creep rupture behaviour as indicated by an intergranular rupture surface located in the HAZ. Detailed metallographic examination is required to obtain an in-depth understanding of metallurgical causes for the occurrence of intergranular HAZ failure.

#### **3.4. The influence of HAZ microstructure on creep rupture**

EBSD mapping was conducted in local areas close to the rupture surface in the HAZ of the specimen tested at 650°C and 160 MPa, Figure 9.

Figure 9 clearly demonstrates the correlation between HAZ microstructure and the location of rupture surface. The surface portion at ~45° to the principal stress direction is close to the boundary between the DZ and the OZ, whereas the portion at ~70° is located within the DZ. The surface portion at ~45° is transgranular and relatively straight (Figures 9a and 9b), whereas the surface portion at ~70° is transformed from intergranular (Figure 9c) to transgranular (Figure 9d) when moving from the region adjacent to the surface



portions at  $\sim 90^\circ$  to the region close to the portion at  $\sim 45^\circ$ . However, the surface portion at  $\sim 90^\circ$  is clearly intergranular and formed along the ‘necklace’ of pre-existing PAGBs as marked by the traces of refined grains  $<20\ \mu\text{m}$  in diameter (Figures 9e and 9f). The location of the intergranular surface portion has been confirmed in the region close to the boundary between the EZ and the DZ, with a distance of  $\sim 1.1\ \text{mm}$  from the fusion boundary. The presence of secondary damage was also observed in the intergranular region on pre-existing PAGBs and triple points (Figures 9f and 9g) in the area close to the rupture surface.

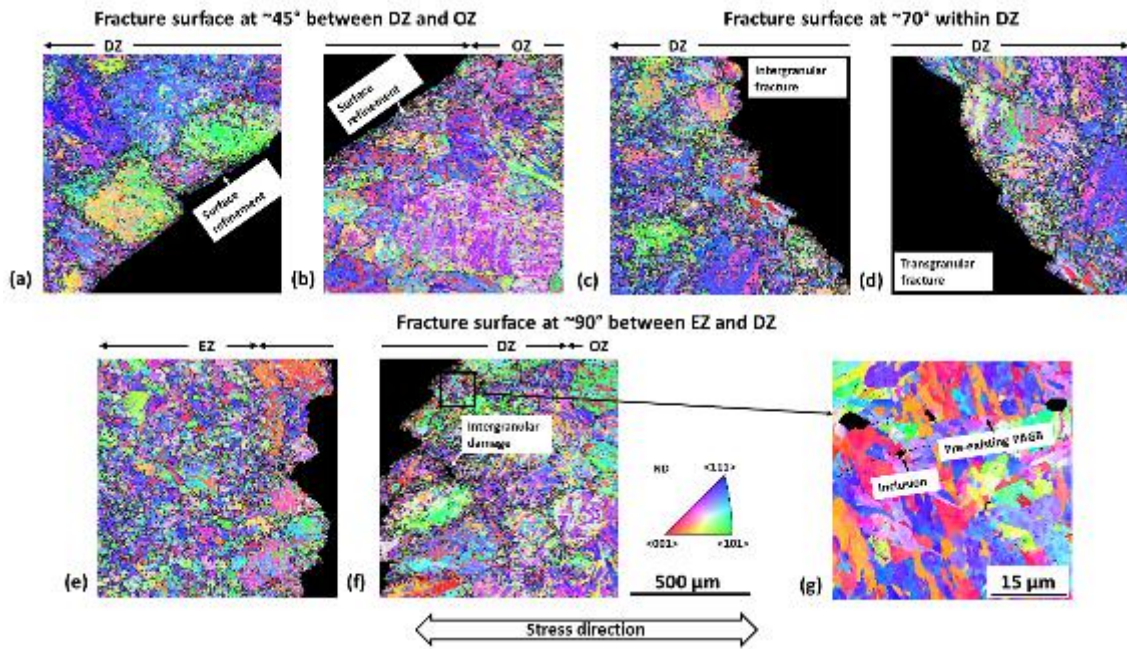
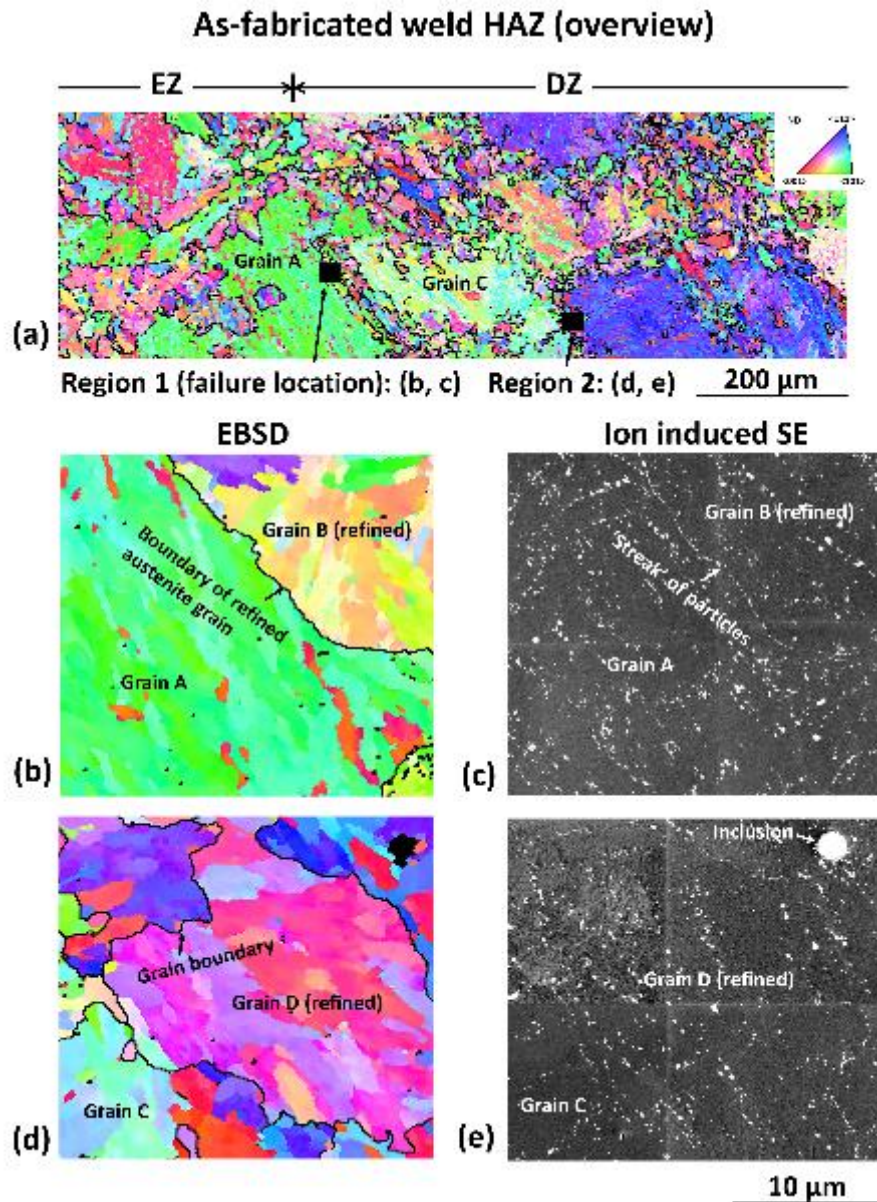


**Figure 9. EBSD maps showing the microstructure in the regions close to rupture surface at (a, b)  $\sim 45^\circ$ , (c, d)  $\sim 70^\circ$  and (e, f)  $\sim 90^\circ$  to the principal stress direction in the specimen tested at  $650^\circ\text{C}$  and  $160\ \text{MPa}$ . (g) An EBSD map collected at a higher resolution detailing the correlation between microstructure and secondary damage close to rupture surface. The grain boundaries with a misorientation range between  $20^\circ$  and  $50^\circ$  are outlined by solid lines.**

The initial microstructure in the HAZ of the as-fabricated IBN-1 weld was further investigated in detail to identify the cause of intergranular creep rupture from a metallurgical perspective. Figure 10 demonstrates the correlative micrographs obtained from the DZ regions in the as-fabricated weld at a similar distance from the fusion boundary as the location of the rupture surface using EBSD and ion induced SE imaging.

Figure 10a demonstrates an evident transition between the EZ and DZ at ~1 mm from the fusion boundary as indicated by the change in microstructure. One region (Region 1) selected for correlative EBSD/ion induced SE analysis is close to the boundary between the EZ and the DZ with a similar distance from the fusion boundary as the rupture surface (Figure 9) to compare with the microstructure in another region (Region 2) further away from the fusion boundary (~1.3 mm). EBSD mapping analysis (Figures 10b and 10d) reveals the elongated blocks that are a few microns in width within the martensitic substructure of the fine and coarse grains within the DZ, whereas the correlative ion induced SE micrographs (Figures 10c and 10e) demonstrate the precipitate particles that are preferentially distributed on substructure boundaries. Notably, the boundary of the refined grains formed along a pre-existing PAGB (e.g. Grain B) are consistently decorated by precipitate particles with a diameter of <150 nm in Region 1 (Figure 10c), whereas the boundary of the refined grains in Region 2 (e.g. Grain D) are decorated to a lesser extent (Figure 10d). This is attributed to an incomplete dissolution of the pre-existing precipitate particles in the regions further away from the fusion boundary due to a lower experienced peak temperature, which consumes the carbide forming elements in the matrix and mitigates a further formation of grain boundary precipitates as previously reported in Grade 92 steel weld [20].



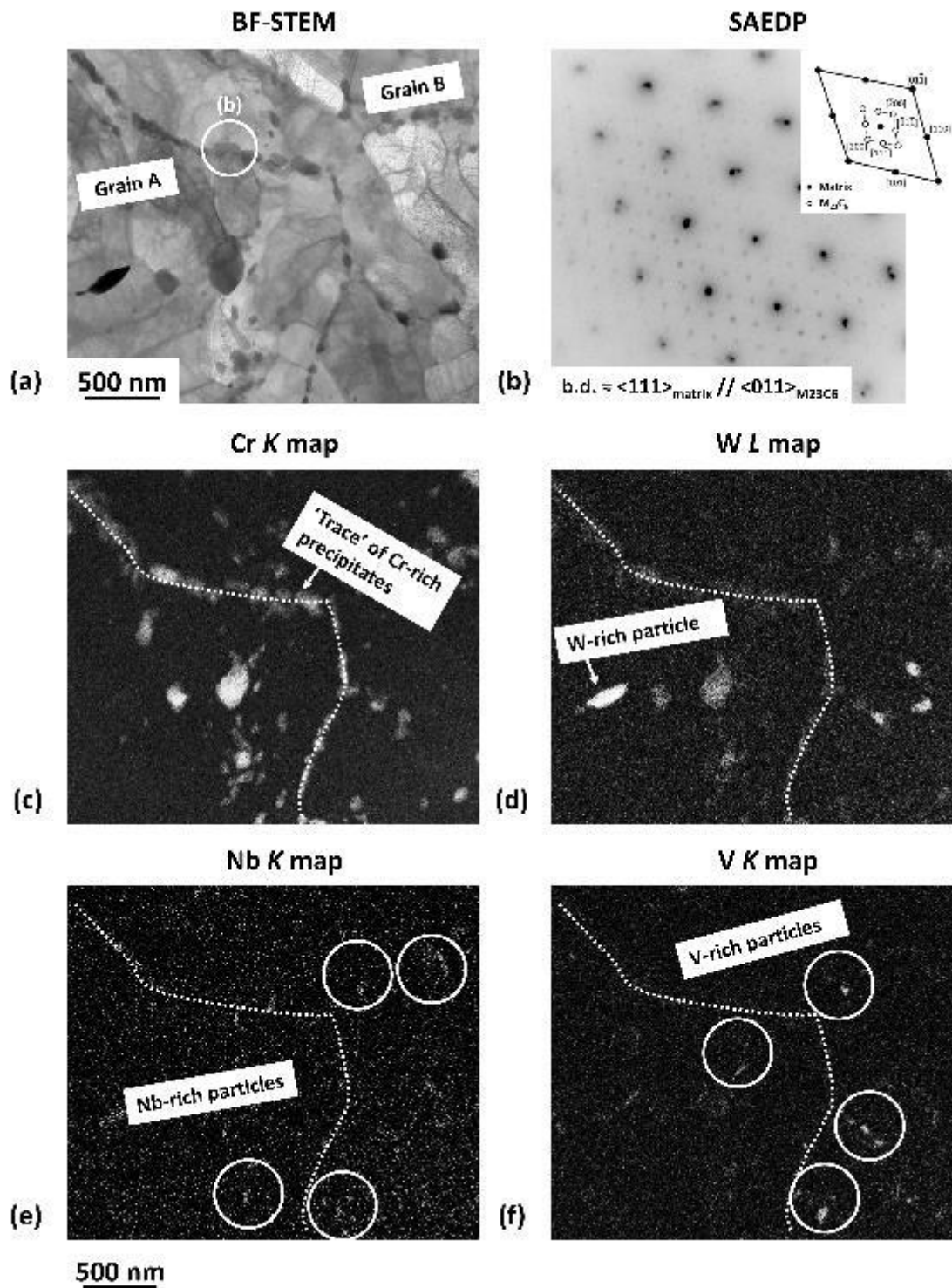
439

440 **Figure 10. (a) A large-scale EBSD map providing an overview of microstructure in**  
 441 **the DZ with the regions of specific analysis indicated by black boxes. (b, d) EBSD**  
 442 **and (c, e) ion induced SE micrographs of the martensitic substructure and the**  
 443 **structure of precipitates in the regions at (b, c) 1.1 mm and (d, e) 1.3 mm from the**  
 444 **fusion boundary. The boundary of small austenite grains on the ‘necklace’ of pre-**  
 445 **existing PAGBs were revealed by a misorientation range of 20°-50°. Ion induced SE**

micrographs were inverted in grey scale for a clear visualisation of the precipitates as bright particles.

The precipitates on the boundary of a refined grain (Grain B) in Region 1 were further extracted using the FIB lift-out technique for high-resolution analysis in TEM using SAED and STEM-EDX. Figure 11 displays a BF-STEM micrograph collected from the boundary of Grain B with the SAEDPs and EDX maps collected from precipitates and the surrounding matrix.

The martensitic substructure is predominantly composed of laths that are  $<1\ \mu\text{m}$  in width in combination with a high density of dislocations within the lath interiors. The majority of the precipitate particles distributed on the boundaries of Grain B are  $<150\ \text{nm}$  in diameter and have an FCC lattice structure similar to the  $\text{M}_{23}\text{C}_6$  carbides [32]. A crystal orientation relationship of  $\{011\}_{\text{precipitate}} // \{111\}_{\text{matrix}}$ ,  $\langle 111 \rangle_{\text{precipitate}} // \langle 011 \rangle_{\text{matrix}}$  was also confirmed between the precipitates and the matrix (Figure 11b). Figures 11c-11f further demonstrate that the precipitates distributed on the boundary of Grain B have a similar chemistry to the  $\text{M}_{23}\text{C}_6$  carbides that are abundant in Cr in combination with a minor level of W [33]. The presence of precipitate particles that are abundant in W or Nb/V was also observed at a minor level (Figures 11d-11f). The chemical compositions of the W-rich and Nb/V-rich precipitates are similar to the chemistry of Laves and MX carbonitrides [34,35], respectively.



465

466 Figure 11. (a) A BF-STEM micrograph of the detailed martensitic microstructure  
 467 in the region adjacent to the boundary of Grain B (Figure 10) and (b) an SAEDP  
 468 collected from a precipitate particle with grey scale inverted for the visualisation of

pattern. (c-f) Correlative EDX maps demonstrating the distribution of elements in the precipitates and the surrounding matrix.

#### 4. DISCUSSION

The dimpled rupture surface on the specimen tested at 650°C and 200 MPa is formed by ductile fracture due to significant stress concentration in the necked region, similar to that as previously observed in parent metal specimens [22]. However, the rupture behaviour of the IBN-1 weld tested at 650°C and 160 MPa is distinctively different and is marked by an intergranular rupture surface located within the HAZ. Based on detailed metallographic examinations of the specimens before and after creep exposure, the rupture surface generated at an applied stress of 160 MPa was found to be located in the region close to the boundary between EZ and DZ.

The EZ and DZ are distinctively classified by an evident transition in prior austenite grain morphology from an equiaxed microstructure to a duplex structure containing refined PAGs distributed on the initial PAGBs (Figure 10). These fine grains are likely to form via a diffusive transformation mechanism that is initiated from the PAGBs due to a lower energy for formation. This is evidenced by a preferential distribution of Cr-containing  $M_{23}C_6$  carbides on the boundary of these refined grains (Figure 10). This is caused by the segregation of carbide forming elements (e.g. Cr) on the boundaries as result of diffusion [38]. Similar observations were also obtained from a Fe-13%Cr-4%Ni-Mo martensitic steel after diffusive austenitisation in the lower temperature regime (i.e. tempering at <680°C) as previously reported [39].

However, it is considered that the materials in the remaining area (i.e. close to the centre of PAGs) are associated with a displacive austenitisation process induced by the rapid



heating rates experienced during welding. The existing observations of displacive austenitisation is comparatively limited for 9-12% Cr steels due to a relatively lower heating rate associated with typical manufacturing and heat treatment processes utilised for industrial applications [40]. However, fusion welding may facilitate the reaustenitisation of original parent metal in the weld HAZ via a diffusionless, displacive mechanism due to a high heating rate associated with weld thermal cycles that is typically  $>100^{\circ}\text{C/s}$  as revealed in previous research [16,18]. The critical threshold of heating rate for the occurrence of displacive austenitisation has been determined to be  $\sim 400^{\circ}\text{C/s}$  in a 0.15%C-5%Mn low alloy steel, whilst displacive austenitisation has been reported upon a heating rate of  $5^{\circ}\text{C/s}$  in a Fe-13%Cr-4%Ni-Mo steel [28,41].

The resultant microstructure formed by displacive austenitisation has been demonstrated in a previous study as a duplicated austenitic structure defined by high-angle PAGBs in combination with austenitic laths sharing similar crystal orientation formed within the PAG interiors. The austenitic laths with a similar crystal orientation are formed within an individual PAG due to a crystallography memory effect that ‘reverses’ the orientation of  $\alpha/\alpha'$ -Fe matrix based on a Kurdjumov-Sachs orientation relationship [42]. In the current research, the microstructure observed from the central area within the PAG interiors in the DZ (Figures 3 and 9) is in strong agreement with the austenitic microstructure formed in a displacive manner as reported in [42]. This also explains the lack of high-angle boundaries within the interiors of pre-existing PAGs in the DZ as highlighted by a range of misorientation of  $20^{\circ}$ - $50^{\circ}$ . Therefore, the duplex austenitic structure in the DZ is formed via a diffusive reaustenitisation process that gives rise to refined grains along the pre-existing PAGBs in combination with a displacive mechanism that reaustenitises the martensitic matrix within the PAG interior. This is consistent with the experimental

observation as previously reported in another MarBN steel [26]. Upon further heating after austenitisation is completed, the displacively formed austenite is prone to recrystallisation due to a high density of dislocations in the microstructure as reported in [41,42]. This further explains the presence of an equiaxed austenitic structure in the regions closer to the fusion boundary as highlighted in the EZ area (Figures 3 and 9).

The martensite transformed from displacively formed austenite is commonly related with a higher dislocation density inherited from the initial austenitic microstructure as compared to the martensitic phases transformed from diffusively formed austenite [41,42]. This suggests a higher dislocation density in the martensitic matrix within the PAG interiors as compared to the intergranular regions showing a refined austenitic structure formed by diffusive phase transformation. Therefore, the intergranular regions along the PAGBs are more susceptible to damage formation by acting as the vulnerable sites in the microstructure. In addition, the correlative EBSD and ion induced SE analysis has revealed preferential formation of the  $M_{23}C_6$  carbides on the boundaries of diffusively formed austenite grains in the region close to the boundary between the EZ and DZ. This is consistent with the observation from a previous study on a Fe-1%Cr-0.6%C alloy that reveals the segregation of Cr accompanied with the migration of austenite grain boundaries during diffusive austenitisation [38]. The diffusion of carbide forming elements away from the pre-existing PAGBs further explains the scarcity of intergranular  $M_{23}C_6$  carbides in the areas between refined austenite grains. The depletion of precipitates on PAGBs may further contribute to a higher susceptibility of intergranular damage due to a lack of stabilisation effect provided by the grain boundary precipitates [33]. Figure 12 demonstrates a schematic diagram illustrating the critical metallurgical factors



associated with the formation of intergranular damage in a duplex martensitic microstructure formed by a combination of diffusive and displacive mechanisms.

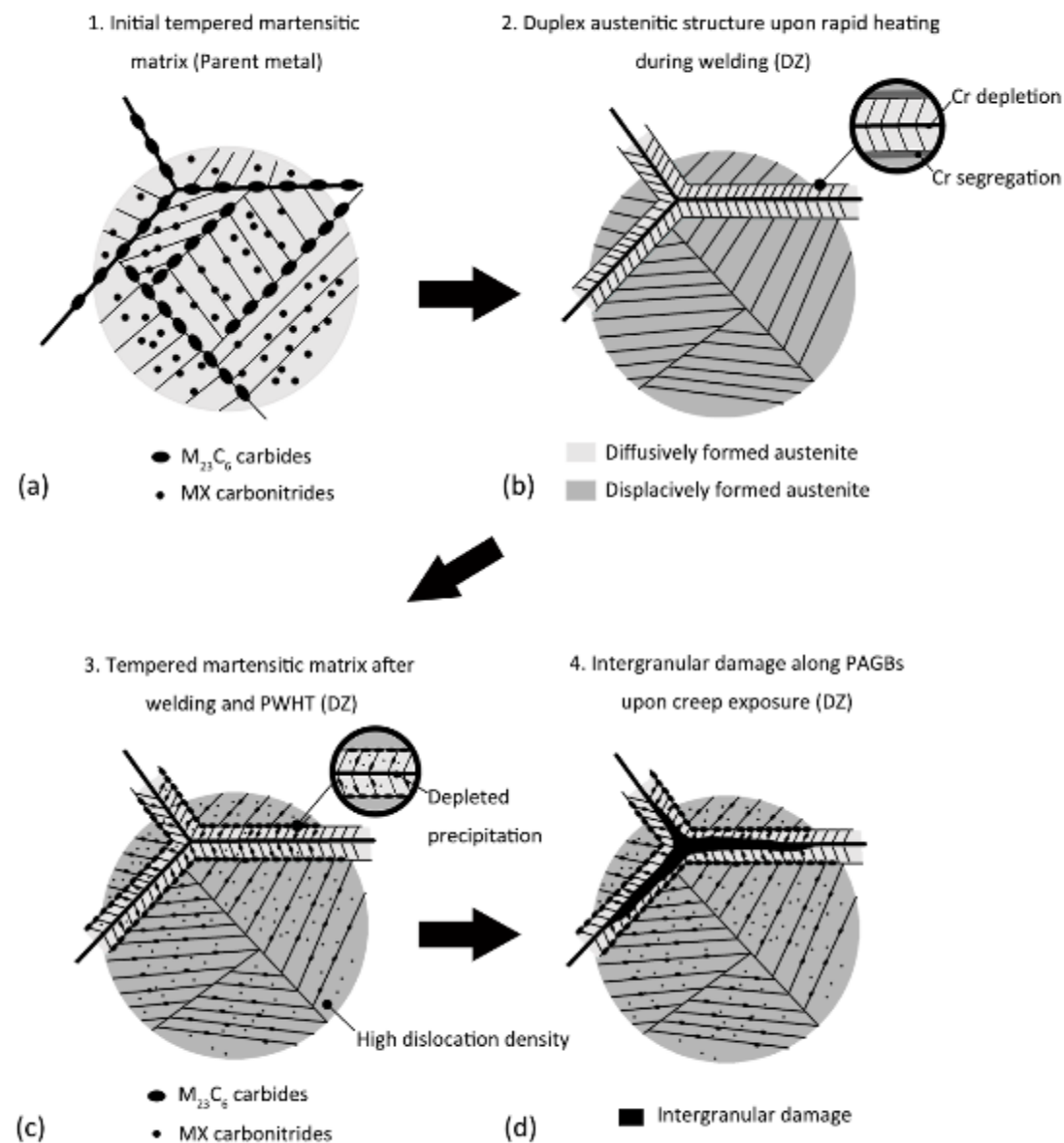


**Figure 12. A schematic diagram illustrating the formation of intergranular damage in the microstructure of DZ after reaustenitisation from the initial microstructure of the parent metal prior to PWHT.**

## 5. CONCLUSIONS

The microstructural distribution in the HAZ of IBN-1 welds has been clearly determined and classified into three distinctive sub-regions as the Equiaxed Zone (EZ), the Duplex Zone (DZ) and the Over-tempered Zone (OZ) in the initial microstructure prior to creep exposure. The microstructural and mechanical characterisations conducted after short-term creep testing have further revealed an evident variation in creep behaviour between the welds tested at different stress levels and the bulk materials tested at identical conditions. From a mechanical point of view, a low creep resistance of the welds, as compared to the parent metal, has been observed. The SSCR values for the welds were found 26-fold higher than the parent metal, while the time to rupture was 14- to 18-fold shorter as compared to the parent metal.

Detailed fractography and metallography examinations revealed a ductile rupture occurred in the parent metal for the welds tested at a higher level of stress, whilst the welds tested at a lower stress demonstrated a failure location in the DZ microstructure close to the boundary with EZ. The initiation of such failure in IBN-1 welds was dominated by intergranular cracking along the pre-existing initial PAGBs from the original microstructure of the parent metal. The areas along these PAGBs acted as vulnerable sites in a tempered martensitic matrix transformed from an austenitic microstructure formed by a combination of diffusive and displacive mechanisms. In particular, the intergranular regions were associated with higher damage susceptibility due to a relatively lower strength as compared to the matrix within the PAG interiors and a lack of precipitates on the PAGBs.

## **6. ACKNOWLEDGMENTS**

This work was supported by the Engineering and Physical Sciences Research Council (<https://www.epsrc.ac.uk/>) through the IMPULSE project (grant number: EP/N509991/1). The authors gratefully acknowledge the following partners for their valuable contributions: Doosan Babcock, GE Power, Uniper Technologies, Metrode Products, Goodwin Steel Castings and Wyman-Gordon. Specific acknowledgments to Dr Paul Robb (Doosan Babcock) for providing the test material and welding procedure. The authors also acknowledge use of facilities within the Loughborough Materials Characterisation Centre.

## **7. DATA AVAILABILITY**

The raw/processed data required to reproduce these findings cannot be shared at this time as the data also forms part of an ongoing study.

## **8. REFERENCES**

- [1] M. Taneike, F. Abe, K. Sawada, Creep-strengthening of steel at high temperatures using nano-sized carbonitride dispersions, *Nature*. 424 (2003) 294–296.
- [2] R. Viswanathan, R. Purgert, U. Rao, Materials technology for advanced coal power plants, in: Proc. 1st Int. Conf. ‘Super-High Strength Steels’, Rome, Italy, 2005.
- [3] T. Hamaguchi, H. Okada, S. Kurihara, H. Hirata, M. Yoshizawa, A. Iseda, Microstructural Evaluation of 9Cr-3W-3Co-Nd-B Heat-Resistant Steel (SAVE12AD) After Long-Term Creep Deformation, in: ASME 2017 Pressure Vessels and Piping Conference, American Society of Mechanical Engineers, 2017.
- [4] S. Hollner, E. Piozin, P. Mayr, C. Caës, I. Tournié, A. Pineau, B. Fournier, Characterization of a boron alloyed 9Cr3W3CoVNbBN steel and further improvement

590 of its high-temperature mechanical properties by thermomechanical treatments, *J. Nucl.*  
591 *Mater.* 441 (2013) 15–23.

592 [5] D.J. Allen, An investigation of the factors determining creep strength and  
593 ductility in Grade 92 steel, in: Kern, T. (ed.) 4th International ECCC Creep & Fracture  
594 Conference (ECCC 2017), Dusseldorf, 10-14th September. Dusseldorf: Steel Institute  
595 VDEh.

596 [6] P. Yan, Z. Liu, H. Bao, Y. Weng, W. Liu, Effect of tempering temperature on  
597 the toughness of 9Cr–3W–3Co martensitic heat resistant steel, *Mater. Des.* 54 (2014)  
598 874–879.

599 [7] F. Masuyama, M. Matsui, N. Komai, Creep rupture behavior of advanced 9-12%  
600 Cr steel weldment, *Key Eng. Mater.* 171 (1999) 99–108.

601 [8] V. Sklenička, K. Kuchařová, M. Svobodová, M. Kvapilová, P. Král, L. Horváth,  
602 Creep properties in similar weld joint of a thick-walled P92 steel pipe, *Mater. Charact.*  
603 119 (2016) 1–12.

604 [9] H.J. Schuller, L. Hagn, A. Woitscheck, Cracking in the Weld Region of Shaped  
605 Components in Hot Steam Pipe Lines–Materials Investigations, *Der Maschinenschaden.*  
606 47 (1974) 1–13.

607 [10] D.J. Abson, J.S. Rothwell, Review of type IV cracking of weldments in 9-12%  
608 Cr creep strength enhanced ferritic steels, *Int. Mater. Rev.* 58 (2013) 437–473.

609 [11] J.A. Francis, W. Mazur, H. Bhadeshia, Review Type IV cracking in ferritic  
610 power plant steels, *Mater. Sci. Technol.* 22 (2006) 1387–1395.

611 [12] J.D. Parker, Creep cavitation in CSEF steels, in: *Proc. Seventh Int. Conf. Adv.*  
612 *Mater. Technol. Foss. Power Plant*, 2013: p. 714.

613 [13] Y. Gu, Microstructural investigation of creep behaviour in Grade 92 power plant  
614 steels, Ph.D. thesis, 2017.

615 [14] Y. Liu, S. Tsukamoto, T. Shirane, F. Abe, Formation Mechanism of Type IV  
616 Failure in High Cr Ferritic Heat-Resistant Steel-Welded Joint, *Metall. Mater. Trans. A*.  
617 44 (2013) 4626–4633.

618 [15] K. Kimura, Y. Takahashi, Evaluation of long-term creep strength of ASME  
619 Grades 91, 92, and 122 type steels, in: ASME 2012 Press. Vessel. Pip. Conf., American  
620 Society of Mechanical Engineers, 2012: pp. 309–316.

621 [16] M.S. L. Havelka, P. Mohyla, Thermal cycle measurement of P92 welded joints,  
622 in: *Proc. 23rd Int. Conf. Met. Mater.*, 2014.

623 [17] A.H. Yaghi, D.W.J. Tanner, T.H. Hyde, A.A. Becker, W. Sun, Abaqus Thermal  
624 Analysis of the Fusion Welding of a P92 Steel Pipe, in: *SIMULIA Cust. Conf.*, 2011:  
625 pp. 622–638.

626 [18] A.H. Yaghi, T.H. Hyde, A.A. Becker, W. Sun, Finite element simulation of  
627 welding and residual stresses in a P91 steel pipe incorporating solid-state phase  
628 transformation and post-weld heat treatment, *J. Strain Anal. Eng. Des.* 43 (2008) 275–  
629 293.

630 [19] X. Xu, G.D. West, J.A. Siefert, J.D. Parker, R.C. Thomson, Microstructural  
631 Characterization of the Heat-Affected Zones in Grade 92 Steel Welds: Double-Pass and  
632 Multipass Welds, *Metall. Mater. Trans. A*. 49 (2018) 1211–1230.

633 [20] X. Xu, G.D. West, J.A. Siefert, J.D. Parker, R.C. Thomson, The Influence of  
634 Thermal Cycles on the Microstructure of Grade 92 Steel, *Metall. Mater. Trans. A*. 48  
635 (2017) 5396–5414.

636 [21] J. Guo, X. Xu, M.A.E. Jepson, R.C. Thomson, Influence of weld thermal cycle  
637 and post weld heat treatment on the microstructure of MarBN steel, *Int. J. Pres. Ves.*  
638 *Pip.* 174 (2019) 13-24.

639 [22] A. Benaarbia, X. Xu, W. Sun, A.A. Becker, M.A.E. Jepson, Investigation of  
640 short-term creep deformation mechanisms in MarBN steel at elevated temperatures,  
641 *Mater. Sci. Eng. A.* 734 (2018) 491-505.

642 [23] L. Li, R. MacLachlan, M. a. E. Jepson, R. Thomson, Microstructural Evolution  
643 of Boron Nitride Particles in Advanced 9Cr Power Plant Steels, *Metall. Mater. Trans.*  
644 *A.* 44 (2013) 3411–3418.

645 [24] L.A. Giannuzzi, B.W. Kempshall, S.M. Schwarz, J.K. Lomness, B.I. Prenitzer,  
646 F.A. Stevie, FIB Lift-Out Specimen Preparation Techniques, in: L.A. Giannuzzi, F.A.  
647 Stevie (Eds.), *Introd. to Focus. Ion Beams Instrumentation, Theory, Tech. Pract.*,  
648 Springer US, Boston, MA, 2005: pp. 201–228.

649 [25] Y. Li, K. Li, Z. Cai, J. Pan, X. Liu, P. Wang, Alloy design of welding filler  
650 metal for 9Cr/2.25 Cr dissimilar welded joint and mechanical properties investigation,  
651 *Weld. World.* 62 (2018) 1137–1151.

652 [26] F. Abe, M. Tabuchi, S. Tsukamoto, Metallurgy of Type IV fracture in advanced  
653 ferritic power plant steels, *Mater. High Temp.* 28 (2011) 85–94.

654 [27] H. Kitahara, R. Ueji, N. Tsuji, Y. Minamino, Crystallographic features of lath  
655 martensite in low-carbon steel, *Acta Mater.* 54 (2006) 1279–1288.

656 [28] N. Nakada, T. Tsuchiyama, S. Takaki, D. Ponge, D. Raabe, Transition from  
657 diffusive to displacive austenite reversion in low-alloy steel, *Isij Int.* 53 (2013) 2275–  
658 2277.

659 [29] C.L. Briant, S.K. Banerji, Intergranular failure in steel: the role of grain-  
660 boundary composition, *Int. Met. Rev.* 23 (1978) 164–199.

661 [30] J. Lin, Y. Liu, T.A. Dean, A review on damage mechanisms, models and  
662 calibration methods under various deformation conditions, *Int. J. Damage Mech.* 14  
663 (2005) 299–319.

664 [31] T. Sakthivel, M. Vasudevan, K. Laha, P. Parameswaran, K.S. Chandravathi, S.P.  
665 Selvi, V. Maduraimuthu, M.D. Mathew, Creep rupture behavior of 9Cr–1.8 W–0.5 Mo–  
666 VNb (ASME grade 92) ferritic steel weld joint, *Mater. Sci. Eng. A.* 591 (2014) 111–  
667 120.

668 [32] A. Baltusnikas, I. Lukosiute, R. Levinskas, Transformation kinetics of M23C6  
669 carbide lattice parameters in low alloyed steel, *Mater. Sci.* 16 (2010) 320–323.

670 [33] F. Abe, Precipitate Design for Creep Strengthening of 9% Cr Tempered  
671 Martensitic Steel for Ultra-supercritical Power Plants, *Sci. Technol. Adv. Mater. Sci.*  
672 *Technol. Adv. Mater.* 9 (2008) 13002–15.

673 [34] L. Cipolla, H.K. Danielsen, D. Venditti, P.E. Di Nunzio, J. Hald, M.A.J.  
674 Somers, Conversion of MX nitrides to Z-phase in a martensitic 12% Cr steel, *Acta*  
675 *Mater.* 58 (2010) 669–679.

676 [35] O. Prat, J. Garcia, D. Rojas, G. Sauthoff, G. Inden, The role of Laves phase on  
677 microstructure evolution and creep strength of novel 9% Cr heat resistant steels,  
678 *Intermetallics.* 32 (2013) 362–372.

679 [36] Z.B. Zhang, O. V Mishin, N.R. Tao, W. Pantleon, Microstructure and annealing  
680 behavior of a modified 9Cr–1Mo steel after dynamic plastic deformation to different  
681 strains, *J. Nucl. Mater.* 458 (2015) 64–69.

682 [37] M.E. Kassner, T.A. Hayes, Creep cavitation in metals, *Int. J. Plast.* 19 (2003)  
683 1715–1748.

684 [38] G. Miyamoto, H. Usuki, Z.-D. Li, T. Furuhashi, Effects of Mn, Si and Cr addition  
685 on reverse transformation at 1073 K from spheroidized cementite structure in Fe–0.6  
686 mass% C alloy, *Acta Mater.* 58 (2010) 4492–4502.

687 [39] Y.Y. Song, X.Y. Li, L.J. Rong, D.H. Ping, F.X. Yin, Y.Y. Li, Formation of the  
688 reversed austenite during intercritical tempering in a Fe–13% Cr–4% Ni–Mo  
689 martensitic stainless steel, *Mater. Lett.* 64 (2010) 1411–1414.

690 [40] D. Richardot, J.C. Vaillant, A. Arbab, W. Bendick, *The T92/P92 book*  
691 Vallourec-Mannesmann tubes, (2000).

692 [41] Y. Song, X. Li, L. Rong, Y. Li, The influence of tempering temperature on the  
693 reversed austenite formation and tensile properties in Fe–13% Cr–4% Ni–Mo low  
694 carbon martensite stainless steels, *Mater. Sci. Eng. A.* 528 (2011) 4075–4079.

695 [42] N. Nakada, R. Fukagawa, T. Tsuchiyama, S. Takaki, D. Ponge, D. Raabe,  
696 Inheritance of dislocations and crystallographic texture during martensitic reversion into  
697 austenite, *ISIJ Int.* 53 (2013) 1286–1288.

698